Nanocomposites of Terbium Sulfide Nanoparticles with a Chitosan Capping Agent for Antibacterial Applications

Eny Kusrini [1,*], Alya Irma Safira [1], Anwar Usman [2], Eko Adi Prasetyanto [3], Khoirina Dwi Nugrahaningtyas [4], Sri Juari Santosa [5] and Lee D. Wilson [6,*]

1. Department of Chemical Engineering, Faculty of Engineering, Universitas Indonesia, Kampus Baru UI Depok 16424, Indonesia
2. Department of Chemistry, Faculty of Science, Universiti Brunei Darussalam, Jalan Tungku Link, Gadong BE1410, Brunei
3. Faculty of Medical, Atma Jaya Catholic University of Indonesia, Jl. Pluit Raya No.2, Penjaringan, Jakarta 14440, Indonesia
4. Department of Chemistry, Faculty of Mathematics and Natural Sciences, Sebelas Maret University, Jl. Ir Sutami No 36A, Surakarta 57126, Indonesia
5. Department of Chemistry, Faculty of Mathematics and Natural Sciences, Universitas Gadjah Mada, Sekip Utara P.O. Box BLS 21, Yogyakarta 55281, Indonesia
6. Department of Chemistry, University of Saskatchewan 110 Science Place, Room 156 Thorvaldson Building, Saskatoon, SK S7N 5C9, Canada
* Correspondence: eny.k@ui.ac.id (E.K.); lee.wilson@usask.ca (L.D.W.); Tel.: +62-21-7863505 (E.K.); +1-306-966-2961 (L.D.W.); Fax: +62-21-7863506 (E.K.); +1-306-966-4730 (L.D.W.)

Abstract: This study aims to investigate the effect of alkaline pH on the bottom-up synthesis of nanocomposites (NCs) containing terbium sulfide nanoparticles (Tb_2S_3 NPs), where chitosan (CS) was employed as a capping agent, along with evaluation of the antibacterial activity of these NCs. The NCs were characterized using spectroscopy (FESEM-EDX, Raman, FTIR, XRD, XPS, and DLS), zeta-potential, and TGA. The results of FE-SEM, XPS, Raman, and FTIR characterization support the formation of $CS-Tb_2S_3$ NPs. A pH variation from 9 to 11 during composite formation was shown to affect the size and composition of NCs. The antibacterial activity of $CS-Tb_2S_3$ NCs was studied by coating onto commercial contact lenses, where the best loading efficiency of NCs was 48%. The NCs prepared at pH 10 (without contact lenses) had greater antibacterial activity against *Staphylococcus aureus*, with a zone of inhibition diameter of 7.15 mm. The coating of NCs onto commercial contact lenses was less effective for inhibition of *Staphylococcus aureus*, in contrast with the greater activity observed for tetracycline. $CS-Tb_2S_3$ NCs offer promising antimicrobial properties that can be further optimized by control of the surface loading and accessibility of Tb_2S_3 NPs through further study of the role of the chitosan capping agent, since steric effects due to CS are likely to attenuate antimicrobial activity via reduced electron transfer in such nanocomposite systems.

Keywords: antibacterial; capping agent; chitosan; contact lens; Tb_2S_3 nanocomposite

1. Introduction

Infections caused by using contact lenses can occur in the cornea, otherwise known as keratitis. The latter results from an inflammation of the cornea caused by bacteria, viruses, and fungi that cause an infection in the eye that triggers inflammation and damage [1]. One of the causes of this disease is infection by *Staphylococcus aureus (S. aureus)*. Bacterial keratitis is a disease caused by a bacterial infection of the cornea, which is caused by bacteria of the genus *Staphylococcus*, which may cause facile and rapid irritation of the cornea, leading to blindness if not treated early [2].

There are reports of cases with patients who have experienced eye complications, such as keratitis, which caused visual disturbances and pain [3]. Cases of bacterial keratitis have been reported due to the improper use of contact lenses. This trend continues to

increase annually in Indonesia, where improper use due to poor hygiene can be traced as the primary source of transmission of eye infections. In particular, the presence of bacterial agents on the lens surface, such as *S. aureus* bacteria, can increase the risk of disease [4].

Metal sulfide nanoparticles (NPs) with variable sizes (ca. 2–20 nm) can serve as semiconductor nanocrystals [5] and are of continued interest in the biomedical field due to their unique electronic and optical properties [6,7]. These types of nanocrystals have the function of simultaneous drug delivery to human tissues and in-vivo imaging probes due to their large surface area. Such types of NPs have high structural stability and antibacterial activity that differs from conventional chemical agents [8–10]. Rare earth elements (REEs), such as lanthanide, have been reported as anti-amoebic agents [11–14], where the terbium complexes have potential utility as anti-amoebic and causative agents for eye keratitis infection [11]. Various antimicrobial agents act by interfering with various pathways: (1) cell wall synthesis, (2) plasma membrane integrity, (3) nucleic acid synthesis, (4) ribosomal function, and (5) folate synthesis [15]. In the case of nanomaterials, iron–oxide NPs coated with dextran reveal strong peroxidase-like activity (cf. Table 1 in [16]) at acidic pH values and target biofilms with high specificity, which also prevent severe dental caries without impact on the surrounding oral tissues in vivo.

Among the various reported methods for the synthesis of NPs, the wet-chemical method is favorable because it is facile with relatively basic equipment requirements [17]. The form and size of the NPs synthesized by this method can be modified by controlling various parameters [18]. Capping agents or additives are employed in the preparation of NPs to maintain stability and prevent the formation of agglomerates [17,18]. Chitosan is an exemplary capping agent for the preparation of NPs in aqueous media. Chitosan is a versatile polysaccharide produced from the partial deacetylation of chitin that yields a biodegradable, biocompatible, and non-toxic biopolymer that has wide utility in advanced biomedical and therapeutic applications [19–23]. Chitosan displays antimicrobial properties, which relate to its glucosamine units and protolytic behavior that favors adhesion to bacterial surfaces with negative surface charges [24]. In turn, chitosan can cause physical damage to the integrity of the plasma membrane, resulting in rupture and cell death, where its use as a capping agent in the formation of nanoparticles relates to its abundant hydroxyl and amine groups.

Based on the need to develop new NPs with tailored properties, we proposed the synthesis of NPs that employ REEs, such as terbium, along with chitosan as a capping agent to address challenges related to nanoparticle stability. Herein, a commercial contact lens was used as a carrier matrix for chitosan-capped Tb_2S_3 (CS-Tb_2S_3) NPs that was adapted from a previous report [14]. Herein, chitosan (CS) serves as a capping agent for synthesis carried out at variable pH (9–11) to improve the nanoparticle stability, along with the antibacterial properties of the Tb_2S_3 NPs. Ophthalmic drug delivery systems in the form of eye drops have a low residence time and bioavailability. It is posited that the prepared NPs in the form of a CS-based composite can adhere favorably to contact lens surfaces to achieve suitable antibacterial properties for potential therapeutic applications [10,14,25].

Table 1. Comparison of the crystallite size for the NPs based on XRD results.

	2θ	θ (rad)	K	λ	FWHM	B (rad)	Crystallite Size (nm)
pH 9	28.4	0.248	0.9	0.154	1.137	0.0198	7.54
pH 10	28.3	0.247	0.9	0.154	1.145	0.0199	7.55
pH 11	29.8	0.260	0.9	0.154	0.836	0.0145	10.3

2. Materials and Methods

2.1. Materials

Terbium nitrate hexahydrate ($Tb(NO_3)_3.6H_2O$) and chitosan were purchased from Sigma-Aldrich (Milwaukee, WI, USA). Sodium sulfide (Na_2S) was purchased from Smart-Lab, (Tangerang Selatan, Indonesia). Ultrapure water was obtained from the Faculty of

Medicine, Universitas Indonesia (Jakarta, Indonesia). Glacial acetic acid, acetone, ammonium hydroxide, monopotassium phosphate, and sodium hydroxide were purchased from Merck (Darmstadt, Germany). Distilled water was purchased from the ROFA Laboratorium Centre, Indonesia. Commercial contact lenses were employed with a hilafilcon material (Indonesia) [14].

2.2. Synthesis of Modified Tb_2S_3 Nanoparticles with Chitosan as Capping Agent

The method for preparing Tb_2S_3 NPs with chitosan as the capping agent follows an adapted method reported by Lim et al. [18]. Chitosan (0.15 g) was dissolved in 40 mL of ultrapure water containing 1% glacial acetic acid. The solution was purged with nitrogen gas for ca. 30 min while stirring. Then, 14.25 mg of terbium trinitrate hexahydrate ($Tb(NO_3)_3.6H_2O$) was added into the solution, which was stirred at room temperature for 2.5 h. Then, Na_2S (0.5 g) was dissolved in 10 mL of ultrapure water and added to the stirred solution of $Tb(NO_3)_3$, followed by the addition of NH_4OH drop-wise until the desired solution pH was reached (pH 9, 10, and 11, respectively). The solution was stirred for 1 h at 35 °C. Then, the mixture was centrifuged at 4000 rpm for 15 min, along with washing (three times) with ultrapure water. Chitosan in ultrapure water (4 mg/mL) containing 1% glacial acetic acid was dissolved, and the resulting solution (10 mL) was added to the centrifuged solution. Finally, the mixture was sonicated for 1.5 h, followed by centrifugation at 4000 rpm for 10 min, along with washing the sonicated solution with ultrapure water and acetone. The solid NPs of Tb_2S_3 were stabilized with chitosan as the capping agent and stored for future use (characterization and antibacterial testing) in ultrapure water. The preparation method for the CS-Tb_2S_3 NPs is outlined in Figure S1 (cf. Supplementary Material).

2.3. Preparation of Tb_2S_3 Nanoparticle Composites for Antimicrobial Testing onto the Contact Lens System

The preparation method for coating the Tb_2S_3 NPs onto the surface of a contact lens employed the method reported by Kusrini et al. [14] with some modifications. Herein, the CS-Tb_2S_3 NPs were dissolved in a phosphate buffer solution (PBS) at pH 7.4, which was prepared by mixing 50 mL of 0.2 M KH_2PO_4 solution with 39.1 mL of 0.2 M NaOH solution with the addition of distilled water to reach a final volume of 200 mL. All prepared solutions were sonicated for 10 min to ensure complete dissolution. The concentration of CS-Tb_2S_3 NPs was variable (0–0.25 mg mL^{-1}), and the optical absorbance was measured using a UV-Vis spectrophotometer (Shimadzu UV-900, Kyoto, Japan) at 217 nm [25] to enable the preparation of a standard calibration curve. The contact lenses were rinsed with distilled water and air-dried prior to coating with the CS-Tb_2S_3 NPs. Then, the contact lens were imbibed in PBS with the NPs for 10 h to enable surface coating. At the end of the loading stage, the lens were removed from the aqueous media and air-dried. The concentration of the CS-Tb_2S_3 NPs during the loading process was monitored in situ by measurement of the optical absorbance of these NPs at 217 nm [25].

2.4. Characterization of CS-Tb_2S_3 Nanocomposites

The characterization of the CS-Tb_2S_3 NPs was carried out by reviewing the stability of the products through chemical composition, shape, and size parameters. The morphology, particle size, and composition of the prepared NPs were analyzed by FESEM-EDX. The size and crystalline structural features were assessed through XRD, while the structure and interaction of the NPs were analyzed by vibrational spectroscopy (Raman and IR). Thermogravimetry analysis (TGA) profiles of the samples were obtained using a TA Instruments Q50 TGA system (New Castle, DE, USA) with a heating rate of 5 °C min^{-1} up to 500 °C with nitrogen as the carrier gas, as described by Dehabadi et al. [26]. In brief, the particle size distribution (PSD) and zeta potential were measured using a Malvern Zetasizer Nano ZS instrument (Malvern Instruments Ltd., Malvern, Worcestershire, UK).

In brief, a fixed amount of the sample (ca. 40 mg) was suspended in 7 mL Millipore water in small glass vials, where aliquots of the suspension were used to measure the

zeta-potential at pH~6.5. The particle size was obtained by measuring the scattered light (θ = 173°) of suspended particles upon illumination with a laser beam, where the CONTIN algorithm was used to obtain the zeta-potential. The particle size and zeta-potential were estimated from triplicate measurements, where average values consisted of at least ten individual runs with an estimated uncertainty of ±5% [26]. The nanocomposite was centrifuged, and the settled particles were withdrawn and dried under an ultra-high vacuum until a constant pressure was reached before being transferred into the XPS chamber. All X-ray photoelectron spectroscopy (XPS) measurements were collected using a Kratos (Manchester, UK) AXIS Supra system at the Saskatchewan Structural Sciences Centre (SSSC) under UHV conditions. This system is equipped with a 500-mm Rowland circle monochromated Al K-α (1486.6 eV) source and a combined hemi-spherical analyzer (HAS) and spherical mirror analyzer (SMA). A spot size of 300×700 microns was used. All survey scan spectra were collected in the -5 to 1200 binding energy range in 1 eV steps with a pass energy of 160 eV. High-resolution scans of 5 regions were also conducted using 0.1 eV steps with a pass energy of 20 eV. An accelerating voltage of 15 keV and an emission current of 10 mA were used for the analysis.

2.5. Performance Test of CS-Tb$_2$S$_3$ Nanocomposites as Antibacterial Agent

Microbial cultures of *S. aureus* were prepared and allowed to age for 24 h. One dosage of a microbial sample was subjected to a diluent (sterile trypticase soy broth) and then homogenized. Transmittance (%T) was measured using a UV-Vis spectrophotometer with a wavelength of 580 nm to 25%T (10^8 CFU/mL) was measured. Each microbial suspension was added to a petri dish (0.2 mL) along with 20–25 mL of trypticase soy agar medium, which was homogenized and then allowed to solidify. The samples in the form of tetracycline as a positive control were prepared on the surface of the media, which were solidified and allowed to stand for 1 h. Then, the test solutions were absorbed and incubated at 30–35 °C for 18–24 h aerobically, where the inhibition zone was evaluated. Tetracycline was used as a standard antibacterial agent and as a positive control (K+) for comparison with the results of the terbium sulfide nanocomposites (NCs) for this study.

3. Results and Discussion

Notwithstanding current potential issues of toxicity of nanomaterials and their utility as therapeutic agents for human health, there remain some knowledge gaps related to their safety in clinical settings. Nonetheless, there is a need to carry out further studies of new biocompatible nanomaterials that possess antibacterial capabilities since such systems represent potential alternatives with multifunctional properties, which include applications for imaging or to address antibiotic-resistant bacterial strains. Hence, this study was focused on the design of CS-Tb$_2$S$_3$ NCs as antibacterial agents to evaluate their utility in a case study for targeting infections to prevent ocular disease such as keratitis. The results and discussion are divided into several sections that detail the characterization of CS-Tb$_2$S$_3$ NCs and an evaluation of their physicochemical and antibacterial properties. We highlight the use of the *Staphylococcus aureus* (*S. aureus*) strain as part of an explorative study to outline the potential utility of CS-Tb$_2$S$_3$ NCs as an emerging class of antibacterial agents.

3.1. Synthesis of CS-Tb$_2$S$_3$ Nanoparticles

The CS-Tb$_2$S$_3$ NPs were prepared using a bottom-up approach through the wet chemical method (cf. Figure S1). The pH ranged from 9 to 11 as a parameter to investigate the role of pH effects on the properties of the prepared Tb$_2$S$_3$ NPs. An increased concentration of the alkaline solution (NH$_4$OH) will reduce solubility and induce precipitation of the NPs, where the resulting saturated solution is colloidal in nature. Chitosan was selected as a capping agent because of its biocompatibility, biodegradability, and non-toxicity. In addition, chitosan can serve to prevent the agglomeration of the resulting NPs due to steric stabilization of the interface (cf. Scheme 1, *vide infra*).
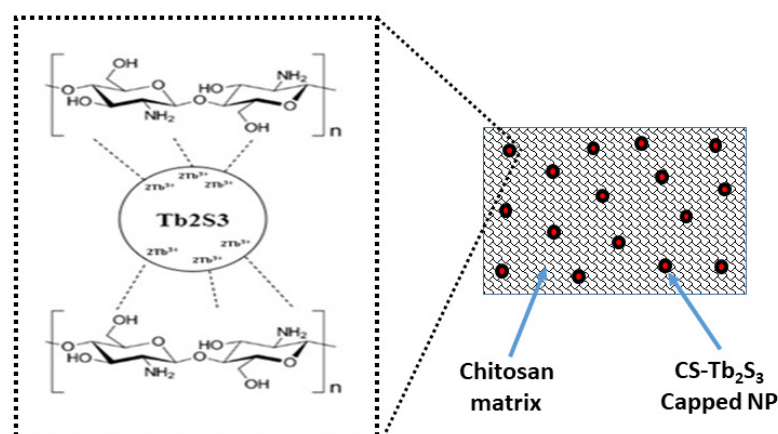
Scheme 1. Conceptual illustration of the structure and interactions for Tb$_2$S$_3$-capped NPs within a chitosan (CS) matrix. The CS shell surrounding the Tb$_2$S$_3$ NP (red sphere) is shown by the use of bold black lines, whereas the microporous CS matrix is shown by the narrow black lines.

3.2. Characterization of the CS-Tb$_2$S$_3$ Nanocomposites

3.2.1. FTIR, Raman, and XPS Structural Characterization

To establish the presence of chitosan and terbium sulfide in the composite material, FTIR spectra were obtained to support the presence of corresponding functional group contributions from the inorganic and organic components.

In Figure 1A, the FTIR spectra for the composites reveal the presence of a new band (500–600 cm^{-1}), which indicates the formation of Tb-S bonds (cf. Figure 1A). The results reported by Rahimi-Nasrabadi et al. [27] revealed that the IR vibrational bands for Tb-S also occur in the 570–800 cm^{-1} region. Herein, the maximum IR intensity of the chitosan band for each NP was reached at pH 11. The peak intensity of the vibrational band of chitosan increased with increasing pH from 9 to 11. Lim et al. [18] reported a similar effect, where chitosan had greater coordination with the NPs at more alkaline pH. In Figure 1B, the Raman spectra of chitosan and the CS-Tb$_2$S$_3$ nanocomposite (pH 10) are presented. There is evidence of spectral intensity variation in the following regions: 2900 cm^{-1}, 1200–1500 cm^{-1}, 800–1200 cm^{-1}, and 300–600 cm^{-1}. While the wavenumber values do not show significant change, the spectral intensities are more pronounced, which suggests that the metal sulfide nanoparticles interact with the accessible functional groups of chitosan (-OH, -NH$_2$) through various donor–acceptor interactions. According to Lim et al. [18], their results reveal that the broad IR band at 420–811 cm^{-1} related to the Cd$_2$S$_3$ vibrational bands, according to the prominent bands at 601 and 720 cm^{-1}, where the arrangement of the biopolymer chains of chitin was relatively unchanged upon encapsulation of the CdS NPs. A more detailed analysis of the Raman spectra in Figure 1B was precluded due to the large fluorescence background emission from the CS-Tb$_2$S$_3$ nanocomposite.

In Figure 1C, XPS was used to confirm the presence of terbium within the chitosan matrix, and XPS was used for elemental identification [28]. Although Tb 4s or Tb 4p$_{3/2}$ are often used to confirm the presence of terbium, the overlap with the N 1s orbital and the C 1s orbital, respectively, from chitosan impedes positive identification and necessitates investigating the Tb 4d, Tb 5p, and Tb 4f orbitals [29]. An added difficulty is the overlap of these orbitals with the silicon contained within the glue on the carbon tape for sample fixation (see Figure 1C). It follows that the changes in peak shape of Si 2s or Tb 4d, respectively. This trend may also originate from other effects that relate to terbium sulfide, which cannot be established unequivocally without confirmation of results from the narrow scan spectra (cf. Figures S4–S11, Supplementary Materials). To elucidate the observed signal and peak identification, the narrow scans of the elements of interest (nitrogen, sulfur, silicon, and terbium) were performed and compared to the narrow scans of the same regions of the carbon tape substrate (cf. Figure 2A–D for narrow scans and Figures S12–S19 in the Supplementary Materials).
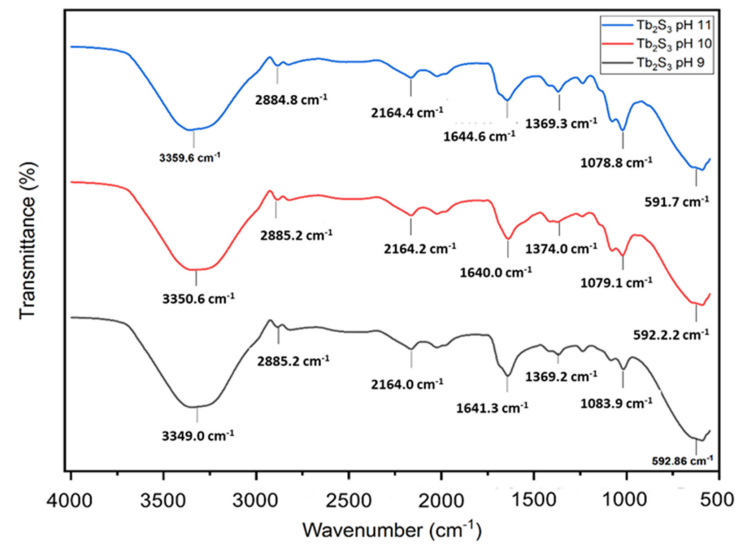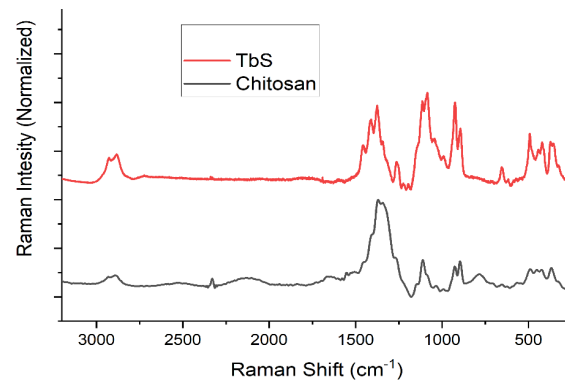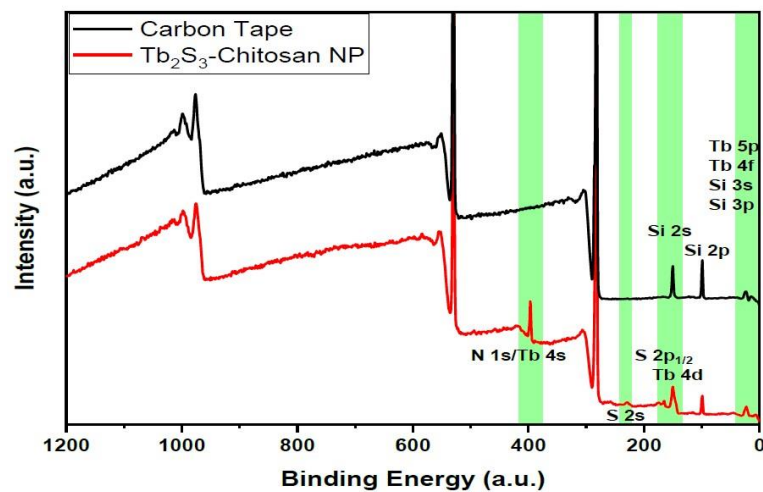
Figure 1. Spectral characterization of CS-Tb$_2$S$_3$ NPs prepared at pH 9–11: (**A**) IR spectra, and (**B**) Raman spectrum of CS-Tb$_2$S$_3$ NPs (pH 10), and (**C**) XPS wide scan spectrum of CS-Tb$_2$S$_3$ NPs (pH 10) and carbon tape.

As can be seen in Figure 2A, the observed peak was not unequivocally identified. The absence of the ammonium band can be explained by the alkali synthetic conditions at pH 10, whereas potentially minor amine peaks around 398.86 eV could be found next to a large band at 396.67 eV, indicating the potential presence of terbium [29]. The narrow

scan of S 2s from sulfur (cf. Figure 2B) indicates a small signal for sulfur, which is absent in the substrate and supports the presence of terbium sulfide. Experimental support is obtained from the deconvolution of the bands for Si 2s and Tb 4 (cf. Figure 2C), where it was possible to identify the silicon band originating from the glue on the carbon tape. The same band is observed in the partially transparent sample, which also reveals the Si 2s (150.42 eV) band, in contrast to the adjacent Tb 4d (144.74 eV and 147.71 eV, respectively) bands. Additionally, the presence of sulfur was confirmed through S 2p in the same region (165.43 eV) [30]. To obtain additional confirmation, the valence electron band spectra (ca. 0–18 eV) were investigated. A sulfur valence band could not be confirmed for S 3p [31]. The Tb 4f orbital around 8 eV was not expected to show overlap with other signals, but most likely silicon also exhibits a peak around 25 eV and smaller peaks between 20 and 0 eV, requiring careful comparison of the peak shapes (cf. Figure 2D). Tb 5p showed too much interference; therefore, the Tb 4f band was used to confirm the presence of terbium sulfide within the NC sample, along with the S 3s peak (18.30 eV), which is absent in the carbon tape. Thus, the elemental identification of terbium within the sample was accomplished by utilizing multiple peaks (Tb 4d, Tb 4f) after deconvolution with overlapping silicon peaks in conjunction with the identification of sulfur peaks (S 2s and S 2p). The oxygen narrow scan (cf. Figure S5 in Supplementary Material) revealed three peaks (528.58 eV, 529.33 eV, and 530.19 eV) in comparison to the two peaks found in the carbon tape (529.43 eV and 530.80 eV; cf. Figure S13 in Supplementary Materials). C-O and C-O-C can be attributed to the latter peaks in both samples, while the peak at 528.58 eV is unique to the terbium sulfide sample, indicating the presence of another oxygen species. This is likely a potential chelation from the C-OH oxygen of chitosan as a hard Lewis base to Tb(III) as the hard Lewis acid [32]. This model of chelation is consistent with the alkaline synthetic conditions (pH 10), where an illustrative view of the interactions between chitosan and terbium sulfide is shown in Scheme 1.
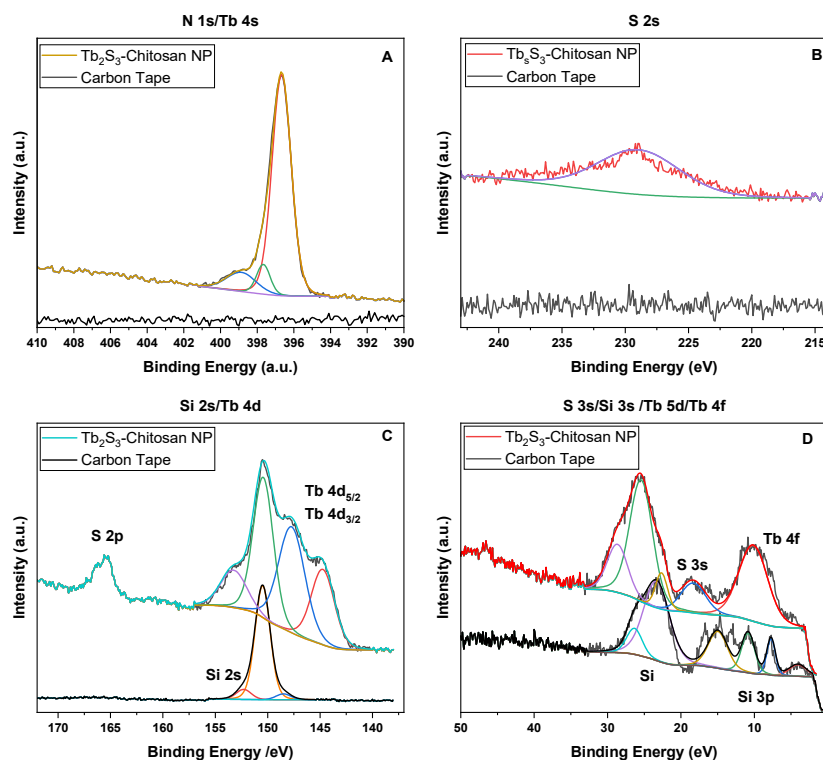
Figure 2. Narrow XPS scans across multiple regions for overlap elucidation and qualitative determination of the composition of the prepared nanoparticles: (**A**). N 1s/Tb 4s; (**B**). S 2s; (**C**). Si 2s/Tb 4d; and (**D**). S 3s/Si 3s/Tb 5d/Tb 4f. The smooth colored lines (red, blue, green, purple) are the best-fit lines for the binding energy of respective atoms to the XPS spectra.

3.2.2. TGA Analysis

Preliminary TGA results in Figure 3A for the CS-Tb_2S_3 NPs (pH 10) reveal two thermal events, both a low temperature event (from 23 °C to 100 °C) and a higher temperature event (ca. centered near 300 °C). The former thermal event relates to water loss, while the latter event relates to chitosan decomposition. Across this range of temperatures investigated, there was no evidence of decomposition due to Tb_2S_3 NPs across this temperature range up to 500 °C. The thermal event near 300 °C provides an estimate of the chitosan content relative to the initial sample weight, after correction for the water content. This method assumes that the residual sample weight after 500 °C is attributable solely to the Tb_2S_3 NPs. The TGA results provide additional support for the formation of a composite between Tb_2S_3 NPs and chitosan as the capping agent.

3.2.3. XRD Analysis

The XRD patterns of CS-Tb_2S_3 NCs prepared at variable pH (9 to 11) are shown in Figure 3B. The presence of XRD signatures at various 2θ values (28.4°, 28.3°, and 29.8°) relates to the monoclinic crystal structure of Tb_2S_3. The Miller indices of each XRD signature are given: (2 3 3) at an angle of 28.43°, (2 4 0) at an angle of 28.28°, and (2 4 2) at an angle of 29.84°, which corresponds to COD no. 432-7787. The broad XRD lines have 2θ values at 29° and 43°, which is in agreement with the signatures reported for chitin and chitosan [33], where chitosan serves as the capping agent and matrix for the terbium sulfide nanoparticles [34].
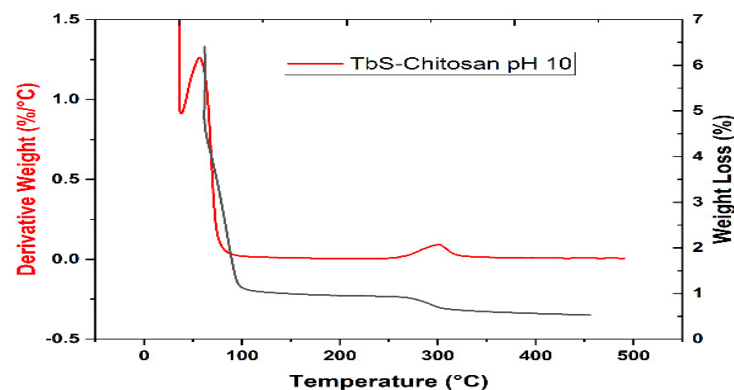
(A)
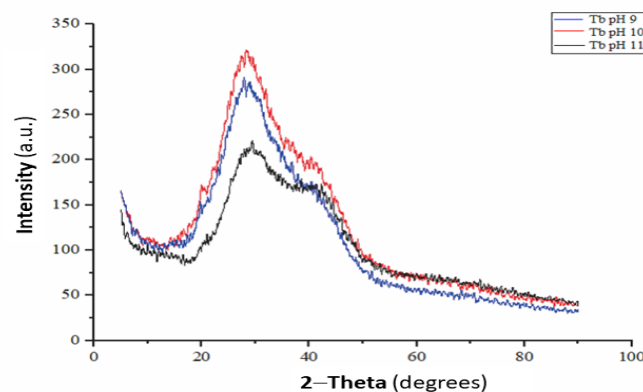
(B)

Figure 3. TGA and XRD profiles for the CS-Tb_2S_3 nanocomposites (pH 10): (**A**) TGA weight loss (%) and derivative weight loss (%/°C), and (**B**) XRD intensity versus 2θ values for nanoparticles prepared between pH 9 and 11.

The size of the Tb_2S_3 nanoparticles was calculated using the Debye–Scherrer equation, $D = (k\lambda/\beta \cos \theta)$, where D is crystallite size, K is known as the Scherrer's constant (K = 0.94), λ is the X-ray wavelength (1.54178 Å), β is full width at half maximum (FWHM) of the diffraction peak. In Table 1, the crystal sizes at variable pH for the CS-Tb_2S_3 NPs are listed based on the XRD line width: 7.53 nm (pH 9), 7.54 nm (pH 10), and 10.28 nm (pH 11).

Taken together, the spectroscopic (XRD, IR, Raman, and XPS) and TGA results provide support that the nanocomposites are comprised of chitosan and terbium sulfide, where the predominant matrix component is chitosan. A conceptual illustration of the interactions between Tb_2S_3 NPs and chitosan (CS) as the capping agent is portrayed in Scheme 1, along with a generalized view of the structure of the CS-Tb_2S_3 nanocomposite.

3.2.4. Particle Size and Zeta-Potential Characterization

Based on the DLS results in Table 2, the particle size for pristine chitosan at alkaline pH ranges from 10^1 to 10^2 μm, where it should be noted that the particle size resides in a range that should not be overinterpreted, according to the larger PDI values near unity. By contrast, the particle diameters estimated for the Tb_2S_3 nanoparticles from XRD range from 7.5 nm to 10.3 nm. The results indicate that the particles in solution estimated by DLS are comprised of chitosan along with multiple components since the particle size of chitosan at pH 3 is two orders of magnitude larger than the lower bound limit obtained by XRD analysis, in accordance with the molecular weight of the capping agent in the 10^2 kD molecular weight range. The anticipated trend of the zeta-potential for chitosan prepared at an alkaline versus an acidic pH is consistent with the positive and negative values in Table 2. For the case of CS-Tb_2S_3 nanocomposites (pH 10), the positive zeta-potential and particle size are consistent with a core-shell morphology (cf. Scheme 1), where chitosan resides at the periphery of the Tb_2S_3 core.

Table 2. DLS and zeta-potential results for chitosan at variable pH and CS-Tb_2S_3 nanoparticles at 295 K.

Sample	Particle Size Z-Average (μm)	PDI	Zeta-Potential (mV)
Chitosan (pH 3)	0.792	0.461	5.11
Chitosan (pH 9)	3.18	1	−2.71
Chitosan (pH 10)	1.82	0.929	−0.614
Chitosan (pH 11)	26.0	0.488	−4.28
CS-Tb_2S_3 NPs (pH 10)	3.64	0.442	12.6

Note: Chitosan is soluble at pH 3 and insoluble at these higher pH values (9–11).

3.2.5. FESEM-EDX Studies

The elemental composition (C, N, O, S, Tb) values of CS-Tb_2S_3 NPs based on the EDX analyses are listed in Table 3.

Table 3. Elemental composition (wt.%) for CS-Tb_2S_3 NPs based on SEM-EDX analyses.

CS-Tb_2S_3 NPs	Weight Composition (wt.%)				
	C	**N**	**O**	**S**	**Tb**
pH 9	49.06	12.06	25.07	9.73	4.08
pH 10	52.09	9.80	28.61	6.45	3.05
pH 11	50.34	11.29	27.44	6.48	4.45

Based on the SEM results, the CS-Tb_2S_3 NPs have small to medium-sized pores and agglomerations, along with some nanofiber structures that resemble the structure of chitosan nanofibers (cf. Figure 3A–C). Image-J software was used for the processing of SEM results to enable size estimates of the terbium sulfide NCs that are present near the

surface. This approach has been widely reported for the study of biological systems [35]. Accordingly, the average particle size for CS-Tb$_2$S$_3$ NCs was estimated for synthesis at variable pH conditions: 57.8 nm (pH 9), 74.9 nm (pH 10), and 114.6 nm (pH 11), as shown in Figure 4a–c. The size range for the Tb$_2$S$_3$ NPs concurs with independent estimates reported elsewhere [36] according to variable particle sizes between 3–80 nm. Some of the NPs reported herein exceed the particle sizes reported by Li et al. [37], which were attributed to agglomeration of Tb$_2$S$_3$ particles as a consequence of the long storage time prior to the FESEM imaging analyses. The composition of the elements in the nanocomposites is outlined in Table 3, where the Tb content was somewhat variable for the systems: 4.08, 3.05, and 4.45 wt.%. In addition, other elements (C, O, N, and S) were detected in the nanocomposites that are related to the presence of chitosan and sulfide.
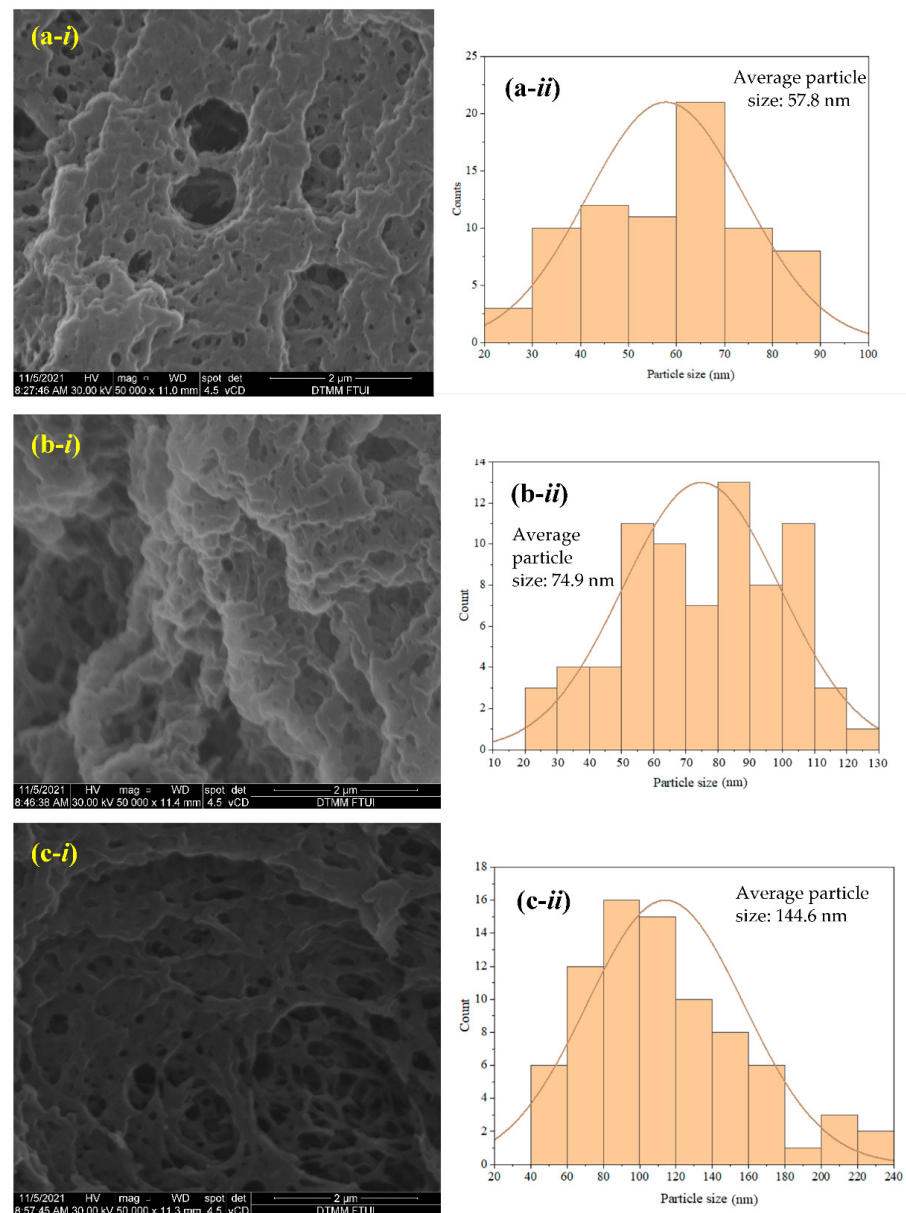
Figure 4. SEM images (**left**) with magnification (50,000×) and 30.0 kV for the CS-Tb$_2$S$_3$ nanocomposites prepared at pH 9 (**a-*i***), pH 10 (**b-*i***), and pH 11 (**c-*i***). The corresponding particle size distribution plots (**right**) were obtained from J-image (*n* = 75 data samples) analysis of SEM results for materials prepared at pH 9 (**a-*ii***), pH 10 (**b-*ii***) and pH 11 (**c-*ii***).

Additional SEM images were obtained at a higher resolution for the chitosan-capped Tb_2S_3 nanoparticles prepared at a pH of 10 (cf. Figure S2, Supplementary Material). Several images of different sample regions (1, 2, and 3) were obtained at greater magnification (150k×) versus the results shown in Figure 4. With reference to Figure S2 (Supplementary Material), where the surface of the sample reveals a number of pseudo-spherical structures in the 10–30 nm size regime across the sample regions (1, 2, and 3). The SEM results indicate evidence of dispersed NPs and aggregated structures at the sample surface, where the light-colored regions reveal emission of secondary electrons, which are attributed to the Tb_2S_3 near the sample interface. The variation of light and dark colored regions is attributed to thinner vs. thicker chitosan shells surrounding the Tb_2S_3 NPs, respectively. This trend concurs with the use of chromium films for contrast image enhancement, along with evidence of Tb species (ca. 0–4 wt.%) based on the EDX analysis of regions 1–3 of the NP domains in Figure S2 (cf. Supplementary Material) and the results are listed in Table 3.

3.3. Antimicrobial Testing of the CS-Tb_2S_3 Nanocomposites

3.3.1. Loading Content of CS-Tb_2S_3 Nanocomposites onto the Contact Lens

The loading content of the NCs onto the contact lens was estimated by calculating the difference between the initial and final concentrations, according to the optical density of the terbium sulfide NPs in aqueous solution. The loading efficiency of CS-Tb_2S_3 NCs onto the contact lens increases non-linearly with the contact time, as shown in Figure S3a (Supplementary Materials). The loading content of the Tb_2S_3 NPs at variable concentrations (0.20 to 0.50 mg mL^{-1}) was evaluated, which is listed in Table 4. The loading efficiencies of CS-Tb_2S_3 NPs onto the surface of commercial contact lens material with an initial concentration of 0.20 to 0.50 mg/mL revealed an increase in loading for NCs that were prepared at variable pH from 9 to 11. The corresponding loading efficiencies are listed: 30%, 43%, and 48%, which increase almost linearly with the concentration of the CS-Tb_2S_3 NCs. The greater loading of the NCs suggests that the particulate uptake onto the contact lens matrix increases with a greater initial NC concentration in the aqueous solution, in accordance with equilibrium considerations. Based on the research of Kaul et al. [35], the results indicated that NPs capped with chitosan had a minimum loading efficiency near 50%. These results also support the fact that the best efficiency in NP stability occurs with chitosan, where a minimum loading occurs near 50%. Thus, it can be assumed that the concentration of CS-Tb_2S_3 NCs ranged from 0.20 to 0.50 mg/mL does not provide effective loading levels required according to conventional standards. The initial concentration of the NCs likely limits the loading efficiency, along with the hydration characteristics of the NCs.

Table 4. Loading efficiency (%) of CS-Tb_2S_3 NPs onto contact lens surfaces.

Initial Concentration (mg/mL)	Final Concentration (mg/mL)	Loading Efficiency (%)
0.20	0.14	30.00
0.30	0.17	43.33
0.50	0.26	48.00

3.3.2. Antibacterial Testing of the CS-Tb_2S_3 Nanoparticles in the Absence and Presence of Contact Lens

For antibacterial activity, the NCs prepared at pH 10 were observed to display an inhibition zone with a diameter of 7.15 mm (cf. Figure 5, dashed red circle). Thus, the CS-Tb_2S_3 NCs prepared at pH 10 were further studied due to the greater antibacterial activity observed. Supporting evidence of the role of terbium species is drawn from a comparison of the antibacterial properties of terbium nitrate salts with other metal salts (zinc nitrate, europium nitrate), as illustrated in Figure S3b,c of the Supplementary Materials.

Based on the data in Table 4, the CS-Tb$_2$S$_3$ NPs had antibacterial activity that resulted in inhibition towards *S. aureus*. The data shows that the presence of an alkaline pH during synthesis and the use of chitosan as the capping agent may contribute secondarily to the overall antibacterial activity. Similar effects were observed by Giridhar et al. [38], Xaba et al. [39], and Ribut et al. [40] for the use of alkaline pH and variable types of capping agents for different types of bacterial strains. We interpret this trend as the optimal formation that favors metal hydroxide surface sites, which enhance the encapsulation of CS-Tb$_2$S$_3$ NPs by chitosan, where it should be noted that the antibacterial contribution of chitosan is considered negligible according to the results presented in Figure S3b,c relative to the greater observed activity of the metal nitrate salts.

The variable concentration of CS-Tb$_2$S$_3$ NCs did not have any notable antibacterial activity, in contrast with tetracycline, which reveals strong inhibition toward *S. aureus* (cf. Table 5). In a study reported by Li et al. [41], they showed that NPs with lanthanide-based materials had antibacterial activity against *S. aureus* when an elevated concentration was employed to inhibit these bacteria.
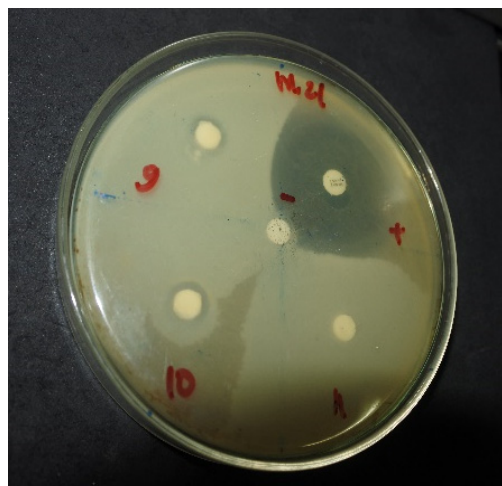
Figure 5. The antibacterial effect of CS-Tb$_2$S$_3$ NCs as antibacterial agents. (+): inhibition and (−): absence of inhibition, where tetracycline was used as a positive (+) control (yellow arrow) and water was used as a negative (−) control in the center of the petri dish.

Table 5. Average diameter of the inhibition zone of CS-Tb$_2$S$_3$ NCs against *S. aureus*.

	Diameter of the Inhibition Zone (mm)			
	pH 9	**pH 10**	**pH 11**	**Tetracycline (K)**
CS-Tb$_2$S$_3$ NPs prepared at pH 10	0.00	7.15	0.00	29.90
	Concentration (mg/mL)			
CS-Tb$_2$S$_3$ NPs prepared at pH 10	0.20	0.30	0.50	Tetracycline (K)
Controls (water, tetracycline)	0.00	0.00	0.00	18.00
CS-Tb$_2$S$_3$ NPs prepared at pH 10 coated on the contact lens	−	−	−	+

(+): inhibition; (−): absence of inhibition, where tetracycline was used as a positive control (K). Tetracycline was used as a positive (+) control and water was used as a negative (−) control.

For the case of commercial contact lenses that were coated with CS-Tb$_2$S$_3$ NPs at a variable concentration (0.20 to 0.50 mg/mL), the antibacterial activity against *S. aureus* was attenuated, which was related to the steric effects of the capping agent. This trend is in contrast with the disc diffusion tests in Figure 5 and greater activity for the tetracycline control system, along with the antibacterial activity of terbium nitrate and negligible activity for chitosan (cf. Figure S3b,c).

A comparison of contact lenses with negative control discs, such as water, reveals the absence of any notable inhibition zone (cf. Figure 5, center of the petri dish). By contrast, tetracycline serves as a positive control, which has a pronounced zone of inhibition (18 mm). However, there was no growth in the media for contact lenses at the low levels of NCs employed. By comparison, higher concentrations revealed a clear, transparent region that denotes bacterial growth inhibition. In turn, we concluded that there was no significant antibacterial activity for the contact lens treated with CS-Tb$_2$S$_3$ NCs, which is contrasted with the results for the tetracycline control (Figure 6). The attenuated antibacterial activity of the NCs relates to several effects, such as the potential release of chitosan over the incubation period (6–10 h), where it is assumed that chitosan begins to break down and or under release from the contact lens. In turn, the concentration of chitosan and terbium sulfide in the form of free CS-Tb$_2$S$_3$ NCs may undergo a decrease due to aggregation effects. The role of adhesion between the contact lens and the CS-Tb$_2$S$_3$ NCs is anticipated to be highly variable due to the steric effects of the capping agent (chitosan) on account of the highly hydrated state (cf. TGA water loss results in Figure 3A) of the system. Hydration effects provide an account of the limited loading efficiency of the CS-Tb$_2$S$_3$ NCs onto the contact lens, in agreement with the loading efficiency in Table 4.

All commercial contact lenses after coating with CS-Tb$_2$S$_3$ NPs at variable concentrations (0.20 to 0.50 mg/mL) did not reveal any notable antibacterial activity against *S. aureus* (cf. Figure 6). Future studies will examine strategies to tailor the stability and adhesion of CS-Tb$_2$S$_3$ NCs onto the surface of the contact lens by variable loading and synthetic conditions to improve the nanoparticle accessibility and the zeta-potential of the capping agent (chitosan) for greater immobilization onto contact lens surfaces to rival the antibacterial properties of the metal salts (cf. Figure S3b,c in the Supplementary Materials) and the CS-Tb$_2$S$_3$ NCs in Figure 7.

This trend supports the proof-of-concept of terbium sulfide NCs as an alternative antibacterial agent (cf. Figure 8). In turn, an improved adhesion of such NCs onto hydrophilic surfaces will afford an alternative treatment strategy for keratitis and related ocular diseases. The favorable hydration properties of the CS-Tb$_2$S$_3$ NPs and the hydrogel material of the contact lenses were inferred to govern the immobilization and antimicrobial properties [42].
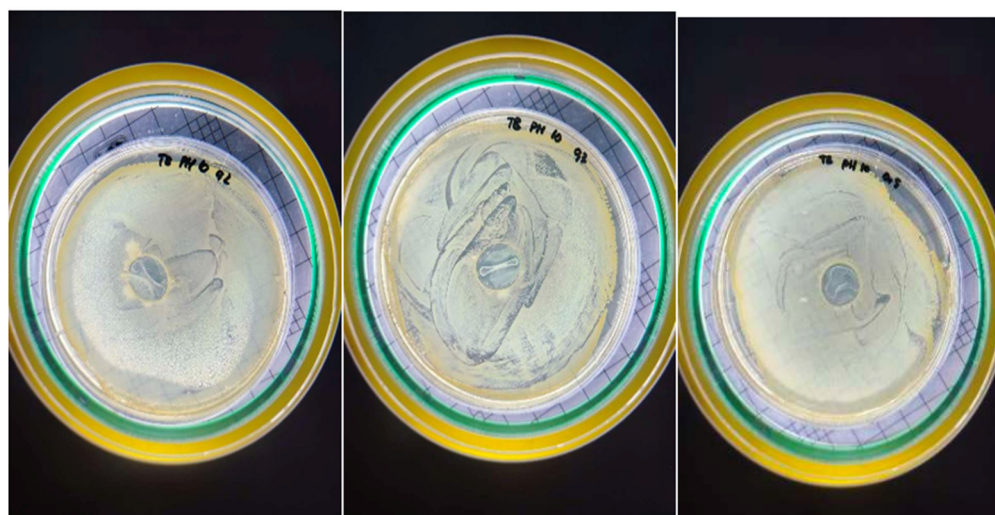
Figure 6. Comparison of the antibacterial tests of the CS-Tb$_2$S$_3$ NCs prepared at a pH of 10 onto contact lens surfaces.
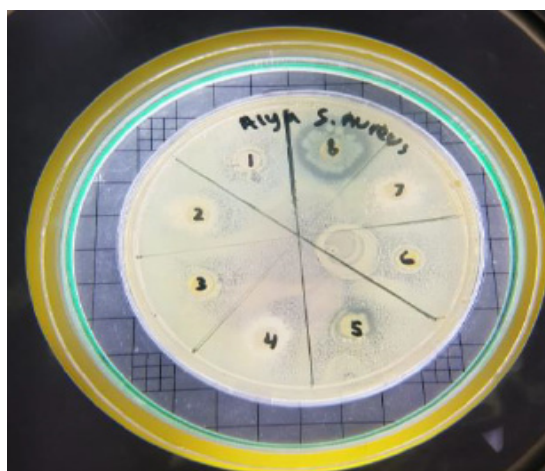
Figure 7. Antibacterial activity of CS-Tb$_2$S$_3$ NCs with variable concentrations: (1) 0.2 mg/mL; (4) 0.3 mg/mL; (7) 0.5 mg/mL. Other numbers (2, 3, 5, and 6) correspond to other metal-based nanoparticle systems (CdS, Ag$_2$S, Eu$_2$S$_3$, ZnS) for comparative purposes. Tetracycline is the positive control (8).
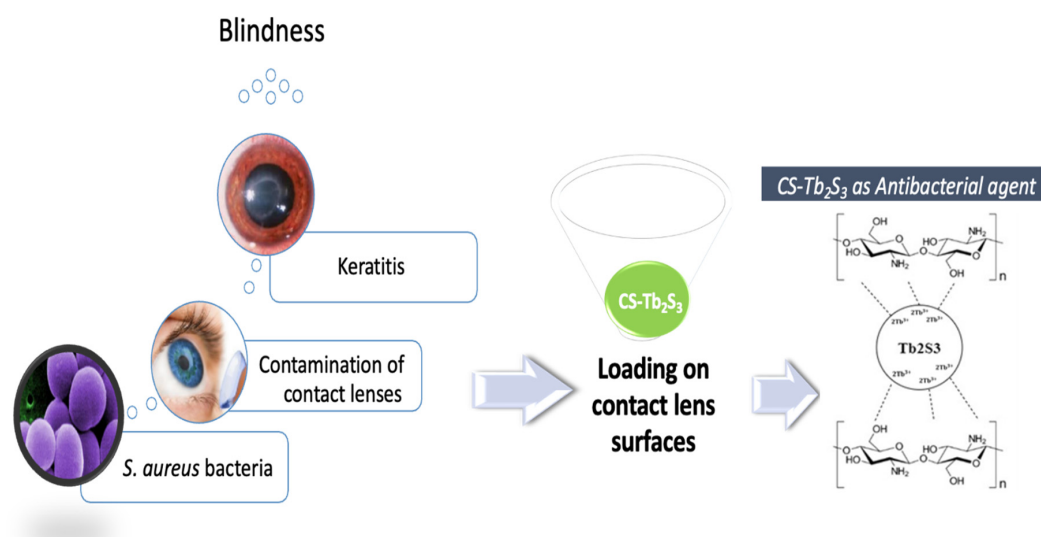
Figure 8. Illustration of contamination of the *S. aureus* bacteria onto contact lenses and treatment using CS-Tb$_2$S$_3$ nanocomposites coated onto contact lens substrates.

4. Conclusions

CS-Tb$_2$S$_3$ nanocomposites (NCs) were successfully synthesized in alkaline media from pH 9 to 11. Variable pH during the NCs synthesis affects the spectral properties (IR, XRD, and DLS) of the resulting materials according to the composition, crystal size, and particle size distribution. IR results reveal a strong spectral band intensity of chitosan with increasing pH, along with increased crystallite size of the CS-Tb$_2$S$_3$ NCs with greater pH during synthesis. The loading efficiencies of CS-Tb$_2$S$_3$ NCs onto commercial contact lenses increased with initial concentrations of 0.2 to 0.5 mg/mL increased, along with greater loading efficiencies of NCs prepared at variable pH: 30% (pH 9), 43% (pH 10) and 48% (pH 11). The CS-Tb$_2$S$_3$ NCs (without contact lenses) inhibited *S. aureus* at pH 10, with an inhibition zone diameter of 7.15 mm. Future work will explore strategies to tailor the capping agent (chitosan) with Tb$_2$S$_3$ NPs, including the conditions for improved immobilization efficiency on contact lenses. In turn, the proof-of-concept of CS-capped NPs to neutralize *S. aureus* bacteria on treated contact lenses was demonstrated. However, greater antimicrobial activity can be achieved through optimization studies since this

exploratory study demonstrates the proof-of-concept. Composites that contain Tb_2S_3 NPs capped with chitosan possess antibacterial properties, which reveal their potential utility for ophthalmic disinfectant applications. This work contributes to the key role of chitosan as a stabilizer agent for NPs and the need to tailor the interfacial properties of such NCs to afford enhanced adhesion at hydrophilic interfaces.

Supplementary Materials: The following supporting information can be downloaded at: https://www.mdpi.com/article/10.3390/jcs7010039/s1. Figure S1 outlines the preparation method and storage of CS-Tb_2S_3 NPs. Figure S2 depicts the SEM of CS-Tb_2S_3 NPs (pH 10) at higher resolution. Figure S3 presents the standard curve of CS-Tb_2S_3 NPs for quantitation studies in phosphate buffer solution and the antibacterial properties of metal nitrate salts toward *E. coli* and *S. aureus*. Figures S4–S11 provide XPS spectra of the nanocomposite prepared at pH 10, and Figures S12–S19 are XPS spectra of carbon tape used for mounting samples.

Author Contributions: Conceptualization, methodology, validation, writing—review and editing, supervision: E.K.; writing—original draft preparation, formal analysis, investigation: A.I.S.; review and editing resources: A.U.; data curation, resources and writing—review and editing: L.D.W.; visualization and project administration: E.A.P., K.D.N. and S.J.S.; Funding acquisition: E.K. All authors have read and agreed to the published version of the manuscript.

Funding: This research was funded by Program Riset Kolaborasi Indonesia-16 PTNBH (RKI), grant number, No. NKB-1065/UN2.RST/HKP.05.00/2022.

Acknowledgments: The authors thank Program Riset Kolaborasi Indonesia-16 PTNBH (RKI), No. NKB-1065/UN2.RST/HKP.05.00/2022. Authors thank Michael from the Department of Biomedicine, Faculty of Medicine and Health Sciences, UNIKA Atma Jaya, and Grace Tania from the Department of Pharmacy, Faculty of Medicine and Health Sciences, UNIKA Atma Jaya. The Saskatchewan Structural Sciences Centre (SSSC) is acknowledged for providing facilities to conduct this research. Funding was received from the Canada Foundation for Innovation, Natural Sciences and Engineering Research Council of Canada and the University of Saskatchewan support research at the SSSC. The following people at the University of Saskatchewan are acknowledged for their technical assistance in data collection: Sarah Purdy is acknowledged for excellent technical assistance with XPS, along with the assistance of Bernd G. K. Steiger with the XPS and TGA results. Deysi J. Venegas-García is acknowledged for technical assistance with particle size and zeta-potential measurements. Loza Taghavi is acknowledged for technical support in Raman spectral results. LDW acknowledges Eiko Kawamura for technical support with SEM imaging at the WCV Image Centre.

Conflicts of Interest: The authors declare no conflict of interest.

References

1. Janumala, H.; Sehgal, P.K.; Mandal, A.B. *Bacterial Keratitis-Causes, Symptoms, and Treatment*; InTech: London, UK, 2012; ISBN 978-953-51-0568-8. Available online: https://cdn.intechopen.com/pdfs/35748/InTech-Bacterial_keratitis_causes_symptoms_and_treatment.pdf (accessed on 6 October 2022).
2. Eltis, M. Contact Lens-related microbial keratitis: Case report and review. *J. Optom.* **2011**, *4*, 122–127. [CrossRef]
3. Rahayu, T.; Menaldi, S.L.; Irawati, Y.; Adriono, G.A.; Presialia, A.; Harini, M.; Friska, D. Validity and reliability of the NEI VFQ-25 questionnaire in Indonesia leprosy patients. *Clin. Epidemiol. Glob. Health* **2022**, *15*, 101039. [CrossRef]
4. Wu, Y.T.-Y.; Willcox, M.; Zhu, H.; Stapleton, F. Contact lenses hygiene compliance and lens case contamination: A review. *Contact Lens Anterior Eye* **2015**, *38*, 307–316. [CrossRef] [PubMed]
5. Thomas, D.; Lee, H.O.; Santiago, K.C.; Pelzer, M.; Kuti, A.; Jenrette, E.; Bahoura, M. Rapid Microwave Synthesis of Tunable Cadmium Selenide (CdSe) Quantum Dots for Optoelectronic Applications. *J. Nanomater.* **2020**, *2020*, 5056875. [CrossRef]
6. Bharali, D.J.; Mousa, S.A. Emerging Nanomedicines for Early Cancer Detection and Improve Treatment. *Pharmacol. Ther.* **2010**, *128*, 324–335. [CrossRef]
7. Sajja, H.K.; East, M.P.; Mao, H.; Wang, A.Y.; Nie, S.; Yang, L. Development of Multifunctional Nanoparticles for Targeted Drug Delivery and Noninvasive Imaging of Theurapeutic Effect. *Curr. Drug Discov. Technol.* **2009**, *6*, 43–51. [CrossRef]
8. Rajendiran, K.; Zhao, Z.; Pei, D.; Fu, A. Antimicrobial Activity and Mechanism of Functionalized Quantum Dots. *Polymers* **2019**, *11*, 1670. [CrossRef]
9. Ames, J.R.; Ryan, M.D.; Kovacic, P. Mechanism of antibacterial action: Electron transfer and oxy radicals. *J. Free Radic. Biol. Med.* **1986**, *2*, 377–391. [CrossRef]
10. Zhou, C.; Wang, Q.; Jiang, J.; Gao, L. Nanozybiotics: Nanozyme-Based Antibacterials against Bacterial Resistance. *Antibiotics* **2022**, *11*, 390. [CrossRef]

11. Kusrini, E.; Hashim, F.; Azmi, W.N.N.W.N.; Amin, N.M.; Estuningtyas, A. A novel anti-amoebic agent against *Acanthamoeba* sp.—A causative agent for eye keratitis infection. *Spectrochim. Acta Part A Mol. Biomol. Spectrosc.* **2016**, *153*, 714–721. [CrossRef]

12. Kusrini, E.; Hashim, F.; Gunawan, C.; Mann, R.; Azmi, W.N.N.W.N.; Amin, N.M. Anti-amoebic activity of acyclic and cyclic-samarium complexes on Acanthamoeba. *Parasitol. Res.* **2018**, *117*, 1409–1417. [CrossRef]

13. Kusrini, E.; Hashim, F.; Saleh, M.I.; Adnan, R.; Usman, A.; Zakaria, I.N.; Prihandini, W.W.; Putra, N.; Prasetyanto, E.A. Monoclinic cerium(III) picrate tetraethylene glycol complex: Design, synthesis and biological evaluation as anti-amoebic activity against *Acanthamoeba* sp. *J. Mater. Sci.* **2020**, *55*, 9795–9811. [CrossRef]

14. Kusrini, E.; Sabira, K.; Hashim, F.; Abdullah, N.A.; Usman, A.; Putra, N.; Prasetyanto, E.A. Design, synthesis and anti-amoebic activity of dysprosium-based nanoparticles using contact lenses as carriers against Acanthamoeba sp. *Acta Ophthalmol.* **2021**, *99*, e178–e188. [CrossRef]

15. Kumar, D.S.; Kumar, B.J.; Mahesh, H.M. Chapter 3-Quantum Nanostructures (NPs): An Overview. In *Synthesis of Inorganic Nanomaterials: Advances and Key Technologies Micro and Nano Technologies*; Woodhead Publishing: Sawston, UK, 2018; pp. 59–88. [CrossRef]

16. Yin, W.; Yu, J.; Lv, F.; Yan, L.; Zheng, L.R.; Gu, Z.; Zhao, Y. Functionalized Nano-MoS$_2$ with Peroxidase Catalytic and Near-Infrared Photothermal Activities for Safe and Synergetic Wound Antibacterial Applications. *ACS Nano* **2016**, *10*, 11000–11011. [CrossRef]

17. Green, M. The nature of quantum dot capping ligands. *J. Mater. Chem.* **2010**, *20*, 5797–5809. [CrossRef]

18. Lim, M.J.; Shahri, N.N.M.; Taha, H.; Mahadi, A.H.; Kusrini, E.; Lim, J.W.; Usman, A. Biocompatible chitin-encapsulated CdS quantum dots: Fabrication and antibacterial screening. *Carbohydr. Polym.* **2021**, *260*, 117806. [CrossRef]

19. Kusrini, E.; Shiong, N.S.; Harahap, Y.; Yulizar, Y.; Dianursanti; Arbianti, R.; Pudjiastuti, A.R. Effects of Monocarboxylic Acids and Potassium Persulfate on Preparation of Chitosan Nanoparticles. *Int. J. Technol.* **2015**, *6*, 11–21. [CrossRef]

20. Usman, A.; Kusrini, E.; Widiantoro, A.B.; Hardiya, E.; Abdullah, N.A.; Yulizar, Y. Fabrication of Chitosan Nanoparticles Containing Samarium Ion Potentially Applicable for Fluorescence Detection and Energy Transfer. *Int. J. Technol.* **2018**, *9*, 1112–1120. [CrossRef]

21. Yan, D.; Li, Y.; Liu, Y.; Li, N.; Zhang, X.; Yan, C. Antimicrobial Properties of Chitosan and Chitosan Derivatives in the Treatment of Enteric Infections. *Molecules* **2021**, *26*, 7136. [CrossRef]

22. Kusrini, E.; Wu, S.; Susanto, B.H.; Lukita, M.; Gozan, M.; Hans, M.D.; Rahman, A.; Degirmenci, V.; Usman, A. Simultaneous Absorption and Adsorption Processes for Biogas Purification using Ca(OH)$_2$ Solution and Activated Clinoptilolite Zeolite/Chitosan Composites. *Int. J. Technol.* **2019**, *10*, 1243–1250. [CrossRef]

23. Kusrini, E.; Ayuningtyas, K.; Mawarni, D.P.; Wilson, L.D.; Sufyan, M.; Rahman, A.; Prasetyanto, Y.E.A.; Usman, A. Micro-structured Materials for the Removal of Heavy Metals using a Natural Polymer Composite. *Int. J. Technol.* **2021**, *12*, 275–286. [CrossRef]

24. Şenel, S.; McClure, S.J. Potential applications of chitosan in veterinary medicine. *Adv. Drug Deliv. Rev.* **2004**, *56*, 1467–1480. [CrossRef]

25. Zhang, J.; Gerile, N.; Davaasambuu, J.; Bolag, A.; Hua, E.; Zhang, Y. Synthesis and Optical Performance of terbium complexes with octanoyl amino acids. *Arab. J. Chem.* **2021**, *14*, 103033. [CrossRef]

26. Dehabadi, L.; Karoyo, A.H.; Soleimani, M.; Alabi, W.O.; Simonson, C.J.; Wilson, L.D. Flax Biomass Conversion via Controlled Oxidation: Facile Tuning of Physicochemical Properties. *Bioengineering.* **2020**, *7*, 38. [CrossRef]

27. Rahimi-Nasrabadi, M.; Pourmortazavi, S.M.; Ganjali, M.R.; Norouzi, P. Nanosized terbium carbonate and oxide particles: Optimized synthesis, and application as photodegradation catalyst. *J. Mater. Sci. Mater. Electron.* **2018**, *29*, 2988–2998. [CrossRef]

28. Moulder, J.F.; Stickle, W.F.; Sobol, P.E.; Bomben, K.D. *Handbook of X-ray Photoelectron Spectroscopy*, 2nd ed.; Chastain, J., Ed.; Perkin-Elmer Corporation: Eden Prairie, MN, USA, 1992.

29. Mohtasebi, A.; Chowdhury, T.; Hsu, L.H.H.; Biesinger, M.C.; Kruse, P. Interfacial Charge Transfer between Phenyl-Capped Aniline Tetramer Films and Iron Oxide Surfaces. *J. Phys. Chem. C* **2016**, *120*, 29248–29263. [CrossRef]

30. Nesbitt, H.W.; Scaini, M.; Höchst, H.; Bancroft, G.M.; Schaufuss, A.G.; Szargan, R. Synchrotron XPS Evidence for Fe^{2+}-S and Fe^{3+}-S Surface Species on Pyrite Fracture-Surfaces, and Their 3D Electronic States. *Am. Mineral.* **2000**, *85*, 850–857. [CrossRef]

31. Pratt, A.; Muir, I.; Nesbitt, H. X-Ray Photoelectron and Auger Electron Spectroscopic Studies of Pyrrhotite and Mechanism of Air Oxidation. *Geochim. Cosmochim. Acta* **1994**, *58*, 827–841. [CrossRef]

32. Pettifer, Z.E.; Quinton, J.S.; Skinner, W.M.; Harmer, S.L. New Interpretation and Approach to Curve Fitting Synchrotron X-Ray Photoelectron Spectra of (Fe,Ni)9S8 Fracture Surfaces. *Appl. Surf. Sci.* **2020**, *504*, 144458. [CrossRef]

33. Anwander, R. *Lanthanides: Chemistry and Use in Organic Synthesis*, 2nd ed.; Kobayashi, S., Ed.; Springer: Berlin/Heidelberg, Germany, 1999; ISBN 9783540698012.

34. Narudin, N.A.H.; Rosman, N.A.; Shahrin, E.W.E.S.; Sofyan, N.; Mahadi, A.H.; Kusrini, E.; Hobley, J.; Usman, A. Extraction, characterization, and kinetics of N-deacetylation of chitin obtained from mud crab shells. *Polym. Polym. Compos.* **2022**, *30*, 1–11. [CrossRef]

35. Kaul, S.; Jain, N.; Pandey, J.; Nagaich, U. Investigating the Retention Potential of Chitosan Nanoparticulate Gel: Design, Development, In-Vitro & Ex-Vivo Characterization. *Recent Pat. Anti-Infect. Drug Discov.* **2020**, *15*, 41–67. [CrossRef]

36. Kurniawan, C.; Waluyo, T.B.; Sebayang, P. Particle size analysis using free-software ImageJ. Seminar Nasional Fisika 2011, Tangerang City, Indonesia, 13–14 July 2011. Available online: https://www.researchgate.net/publication/215445823_Particle_Size_Analysis_Using_Free-Software_ImageJ (accessed on 6 October 2022).

37. Li, X.-B.; Liu, S.; Cao, X.-J.; Zhou, B.-B.; Chen, L.; Yan, A.-R.; Yan, G.-L. Effects of terbium sulfide addition on magnetic properties, microstructure and thermal stability of sintered Nd–Fe–B magnets. *Chin. Phys. B* **2016**, *25*, 077502. [CrossRef]

38. Giridhar, M.; Naik, H.S.B.; Prabhakar, M.C.; Naik, M.M.; Ballesh, N.; Mahesh, M.C. Synthesis, characterization and antibacterial activity of water-soluble dye-capped zinc sulphide nanoparticles from waste Zn–C battery. *Bull. Mater. Sci.* **2021**, *44*, 6. [CrossRef]

39. Xaba, T. Green synthesis of ZnS nanoparticles and fabrication of ZnS–chitosan nanocomposites for the removal of Cr(VI) ion from wastewater. *Green Process. Synth.* **2021**, *10*, 374–383. [CrossRef]

40. Ribut, S.H.; Che Abdullah, C.A.; Mustafa, M.; Mohd Yusoff, M.Z.; Ahmad Azman, S.N. Influence of pH variations on zinc oxide nanoparticles and their antibacterial activity. *Mater. Res. Express* **2018**, *6*, 025016. [CrossRef]

41. Li, C.; Sun, Y.; Li, X.; Fan, S.; Liu, Y.; Jiang, X.; Yin, J.-J. Bactericidal effects and accelerated wound healing using Tb_4O_7 nanoparticles with intrinsic oxidase-like activity. *J. Nanobiotechnol.* **2019**, *17*, 54. [CrossRef]

42. Dehabadi, L.; Karoyo, A.H.; Wilson, L.D. Spectroscopic and Thermodynamic Study of Biopolymer sorption Phenomena in Heterogeneous Solid−Liquid Systems. *ACS Omega* **2018**, *3*, 15370–15379. [CrossRef]